Acta Cryst. (1998). D**54**, 200–214

Stationary Crystal Diffraction with a Monochromatic Convergent X-ray Source and Application for Macromolecular Crystal Data Collection

JOSEPH X. HO,[a]† EDDIE H. SNELL,[a] R. CHARLES SISK,[a] JOHN R. RUBLE,[a]† DANIEL C. CARTER,[a]† SCOTT M. OWENS[b]‡ AND WALTER M. GIBSON[b]

[a]*ES 76 Marshall Space Flight Center, NASA, Huntsville, Alabama 35812, USA, and* [b]*Center for X-ray Optics, State University at Albany, Albany, New York 12222, USA. E-mail: efe@zenith.umdnj.edu*

(Received 23 October 1997; accepted 17 June 1997)

Abstract

A diffraction geometry utilizing convergent X-rays from a polycapillary optic incident on a stationary crystal is described. A mathematical simulation of the resulting diffraction pattern (in terms of spot shape, position and intensity) is presented along with preliminary experimental results recorded from a lysozyme crystal. The effective source coverage factor is introduced to bring the reflection intensities onto the same scale. The feasibility of its application to macromolecular crystal data collection is discussed.

1. Introduction

Recent developments of polycapillary optics with X-ray bending capability (Kumakhov & Kumarov, 1990) has inspired a number studies to explore its applications (Xiao & Poturaev, 1994; Ullrich *et al.*, 1995; Downing, Gibson & MacDonald, 1996). Polycapillary optics can collect X-rays from a divergent source over a wide solid angle and focus them onto the sample thus increasing the flux when compared with conventional data-collection methods (Owens *et al.*, 1996). Conventional data-collection methods (*e.g.* most commonly oscillation) for macromolecular crystals use highly collimated X-ray beams in order to reduce spot overlapping on the detector. This study explores the feasibility of applying convergent/divergent beam optics to macromolecular crystal data collection. Since the beams converge at the crystal and diverge afterwards, the words converge and diverge will be used, respectively, depending upon which side of the crystal the beam is being referred to. In this diffraction method, the crystal remains stationary whilst it is exposed to the convergent beam. The crystal is rotated between exposures in order to get a 'complete' data set.

Data collection for macromolecular crystals utilizing beams with one-dimensional convergence has been produced (Wyckoff & Agard, 1977), but not developed as a routine data-collection method. The technique used a stationary crystal exposed to X-ray from a line focus source. The resulting diffraction pattern resembled that of an oscillation film. In this current study, the crystal is also stationary, but it is exposed to X-rays from a polycapillary optic with two-dimensional convergence. The resulting diffraction pattern resembles that of a summation of screenless precession images at varying small precession angles. The main effect of beam convergence/divergence on the diffraction spots is tangential elongation for a flat detector at a swing angle of zero. Our approach to analyzing the beam-divergence effect can also be applied to other diffraction geometries. This article deals with the method of analyzing diffraction patterns of convergent beams, some simulation results, and preliminary experimental diffraction patterns. Practical software for data processing has yet to be developed.

2. Diffraction geometry

In order to understand the diffraction pattern of a stationary crystal irradiated by a monochromatic convergent beam, we shall divide the beam into many thin concentric conic shells. We will consider only the case where the beams focus at the crystal and are circularly polarized, and where there is no beam aberration. Throughout the text, the angle between the central 'straight through' beam and the most convergent beam is referred to as the convergence/divergence angle, μ_{max}; while the maximum angle between the two extreme beams of the source is referred to as the source angular spread. For a circularly symmetrical source, as in this case, they differ by a factor of two.

For a shell of conic beams with convergent angle μ, if one traces each beam successively around the conic shell surface and uses the observer's moving frame as the frame of reference, then the crystal processes around the direct beam with a constant tilt angle just as it does in a precession experiment with a collimated beam in the laboratory reference frame. Thus, the reciprocal lattice points pass through the Ewald sphere in the same way as in a precession experiment. If one uses a flat area detector to record the diffraction pattern, the pattern will resemble

† Current address: New Century Pharmaceuticals, Inc., 895 Martin Road, Huntsville, AL 35824, USA.

‡ Current address: Quantum Metrology Group, NIST 221/A149, Gaithersburg, MD 20899, USA.

ISSN 0907-4449

that of a screenless precession film with a subtle but important difference. In a precession experiment, the direct beam intercepts the detector at the same detector position while the detector processes with the crystal, however, in this case, each conic shell intercepts the detector with the direct beam positions forming a circle around the detector center with a radius of $r = D\tan\mu$, where D is the crystal-to-detector distance.

Summing up the diffraction from all the conic shells gives the diffraction pattern for a convergent beam measurement. Because of the similarity to the precession method, it has been referred to as spiral precession (Wyckoff & Agard, 1977). The precession method has been well studied and is understood (Buerger, 1964; Xuong & Freer, 1971), however, owing to the above mentioned important difference between the two methods, the convergent beam diffraction pattern cannot be simply thought of as a summation of patterns from successive screenless precisions of varying angles.

For convenience of discussion, we will use a Cartesian system with $Å^{-1}$ as units such that the X axis coincides with the central beam, the Z axis coincides with the goniostat ω axis and the origin is O^* at the crystal, so that the central beam origin O has Cartesian coordinates of $(-\lambda^{-1},0,0)$, in the way a conventional Ewald diagram is constructed. Because of the convergent beams, there are many beam origins lying on a sphere centered on O^* with a radius of λ^{-1} within the convergent cone (Fig. 1), this circular sphere element will be referred to as the 'sphere element of beam origins'.

2.1. *Reciprocal lattice points involved in diffraction*

For a convergent beam incident on a stationary crystal with a convergence angle μ_{max}, the region of the reciprocal space that is involved in diffraction is equivalent to that of a screenless precession at a precession angle μ_{max}. Let us consider a conic shell of the source with beam convergence angle of μ. The X coordinates of the beam origins are all equal to $-(\lambda^{-1}\cos\mu)$. Therefore, for any reciprocal lattice point P with its X coordinate, X_p, the necessary condition for diffraction to happen is,

$$X_p + \lambda^{-1}\cos\mu \le \lambda^{-1},$$

or

$$X_p \le \lambda^{-1}(1 - \cos\mu). \tag{1}$$

If this condition is not satisfied, (*i.e.*, the distances between the reciprocal lattice point and the beam origins are all larger than λ^{-1}) the point does not locate on any of the Ewald spheres centered on the beam origins hence it is not involved in diffraction. Secondly, for any reciprocal lattice point P, there is a plane passing through points O, O^* and P. Out of all the beam origins on the conic shell, the two extreme ones O' and O'' (one is the nearest, the other most distant) are also located on this plane. The intersections of this plane with the two Ewald spheres centred on O' and O'' are two circles with the same radius, λ^{-1} (Fig. 2). If point P is involved in diffraction, it must lie in the shaded area between the two circles, or satisfy the relationship,

$$|O'P| \le \lambda^{-1} \le |O''P|. \tag{2}$$

As in the precession method, this shaded area is rotationally symmetrical around the X axis. $|O'P|$ and $|O''P|$ can be easily calculated by the law of cosines,

$$\begin{aligned}|O'P|^2 &= |O'O^*|^2 + |O^*P|^2 \\ &\quad - 2|O'O^*||O^*P|\cos(\angle OO^*P - \mu) \\ |O''P|^2 &= |O''O^*|^2 + |O^*P|^2 \\ &\quad -2|O''O^*||O^*P|\cos(\angle OO^*P + \mu).\end{aligned}$$

Recognizing that $|O'O^*| = |O''O^*| = \lambda^{-1}$, $|O^*P| = \rho$ and $\angle OO^*P = \arccos(-X_p/\rho) = \beta$, we have

$$|O'P|^2 = \lambda^{-2} + \rho^2 - 2\lambda^{-1}\rho\cos(\beta - \mu) \tag{3}$$

$$|O''P|^2 = \lambda^{-2} + \rho^2 - 2\lambda^{-1}\rho\cos(\beta + \mu), \tag{4}$$

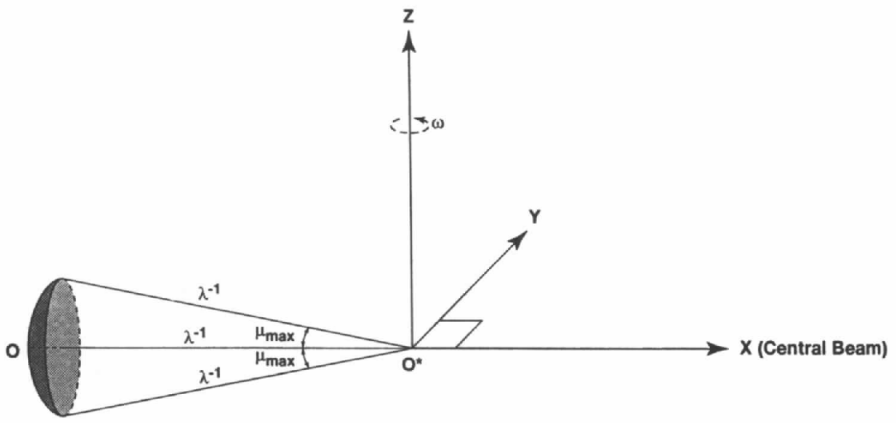

Fig. 1. The Cartesian coordinate system used. The origin is at the reciprocal space origin O^*, with the X axis along central direct beam, and Z axis along the goniostat ω rotation axis. The convergent beam origins are shown as a sphere element within a cone of μ_{max} convergent angle. The sphere element is centered on the reciprocal space origin O^* with a radius of λ^{-1}. Curvature of the sphere element is exaggerated, as is the convergence angle μ_{max}.

where $\rho = (X_p^2 + Y_p^2 + Z_p^2)^{1/2}$. It is easy to understand that larger μ value is associated with a larger reciprocal-space coverage which contains the coverage for all smaller μ's. Thus, we should use the μ value of the outermost conic shell, μ_{max}, for all the above conditions, *i.e.*,

$$|O'P|^2 = \lambda^{-2} + \rho^2 - 2\lambda^{-1}\rho\cos(\beta - \mu_{max}) \quad (5)$$

$$|O''P|^2 = \lambda^{-2} + \rho^2 - 2\lambda^{-1}\rho\cos(\beta + \mu_{max}). \quad (6)$$

Inserting (5) and (6) into (2) and rearranging leads to

$$\cos(\beta + \mu_{max}) \leq \rho\lambda/2 \leq \cos(\beta - \mu_{max}). \quad (7)$$

2.2. *Diffraction conditions of the source origins*

For a reciprocal lattice point P involved in diffraction, *i.e.* satisfying the above conditions [(7)], let us consider which part of the source satisfies the diffraction conditions. This is equivalent to finding the orientations of the crystals at which a reciprocal lattice point satisfies the diffraction conditions in moving crystal methods. For ease of discussion, we will define a cylindrical coordinate system (X, R, φ) with origin at O^* such that

$$\begin{cases} X_p &= X_p \\ R_p &= (Y_p^2 + Z_p^2)^{1/2} \\ \varphi_p &= \arctan(Z_p/Y_p) \\ Y_p &= R_p\cos\varphi_p \\ Z_p &= R_p\sin\varphi_p \\ \rho &= (X_p^2 + Y_p^2 + Z_p^2)^{1/2} = (X_p^2 + R_p^2)^{1/2} \end{cases} \quad (8)$$

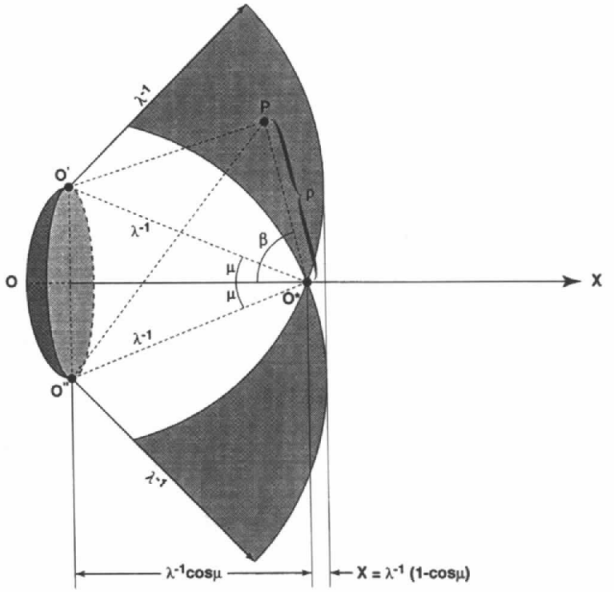

Fig. 2. The region of reciprocal space involved in diffraction. The region is rotationally symmetrical around the X axis. Curvature of the sphere element is exaggerated, as is the convergence angle μ_{max}.

Similarly, for any beam origin, O_s, on the conic shell surface, we have

$$\begin{cases} X_s &= -\lambda^{-1}\cos\mu \\ Y_s &= \lambda^{-1}\sin\mu\cos\varphi_s \\ Z_s &= \lambda^{-1}\sin\mu\sin\varphi_s. \end{cases} \quad (9)$$

Then, the diffraction condition is that,

$$(X_s - X_p)^2 + (Y_s - Y_p)^2 + (Z_s - Z_p)^2 = \lambda^{-2}. \quad (10)$$

Inserting the cylindrical coordinate expressions into the above diffraction condition equation gives (*cf. Appendix A*),

$$\cos(\varphi_p - \varphi_s) = (\rho^2 + 2X_p\lambda^{-1}\cos\mu)/(2R_p\lambda^{-1}\sin\mu). \quad (11)$$

Solutions for this equation exist if and only if the magnitude of the right-hand side of the equation is no greater than unity. The physical significance of this restriction is that for a particular reciprocal point P, there also exists a minimum value of μ (*cf. Appendix A*),

$$\mu_{min} = |\arccos(\rho\lambda/2) - \beta|, \quad (12)$$

source origins contributing to this reflection all lie in the conic shell with convergence angles ranging from μ_{min} to μ_{max}.

Since the cosine function is an even function, there are generally two solutions for φ_s, which we name as φ_n and φ_x analogous to 'entry' and 'exit' points in precession. Then we have,

$$\varphi_n = \varphi_p - \arccos[(\rho^2 + 2X_p\lambda^{-1}\cos\mu)/(2R_p\lambda^{-1}\sin\mu)] \quad (13)$$

$$\varphi_x = \varphi_p + \arccos[(\rho^2 + 2X_p\lambda^{-1}\cos\mu)/(2R_p\lambda^{-1}\sin\mu)]. \quad (14)$$

If one traces all the beams within the convergent beam cone, and uses the moving observer's frame as the frame of reference, then, for any reciprocal lattice point P involved in diffraction, at varying μ angles between μ_{max} and μ_{min}, the trace of points where P intersects the reflecting sphere forms two arcs of a planar circle. This is because of the constraints of the spot on the reflection sphere while maintaining a constant distance ρ from the reciprocal-space origin O^*. The two arcs merge into one at $\mu = \mu_{min}$ [(11) equals 1, or -1, hence $\varphi_n = \varphi_x = \varphi_p$, or $\varphi_n = \varphi_x = \varphi_p + \pi$]. When using a flat detector at 2θ swing angle zero to record the diffraction, the spot shape shows nearly tangential elongation in such a way as to form a conic curve with its midpoint slightly closer to the detector center, *i.e.*, the curvature center of the conic curve pointing away from the detector center. Details of the spot-shape analysis are given later.

2.3. *Detector coordinates*

In the laboratory frame of reference, the reciprocal lattice point P is stationary while diffraction occurs from different parts of the source. Thus, for every μ between μ_{max} and μ_{min}, there are two source origins, O_n and O_x, responsible for diffraction. At $\mu = \mu_{min}$, O_n coincides with O_x ($\varphi_n = \varphi_z$). A typical polar coordinate plot of φ_n, φ_x against μ is shown in Fig. 3. In the laboratory frame of reference, the traces of O_n's and O_x's also form a planar circle, as explained later. The Cartesian coordinates for O_n at various μ angles are simply,

$$\begin{cases} X_n &= -\lambda^{-1}\cos\mu \\ Y_n &= \lambda^{-1}\sin\mu\cos\varphi_n \\ Z_n &= \lambda^{-1}\sin\mu\sin\varphi_n. \end{cases} \tag{15}$$

We will adopt the same Cartesian system for the real space, but with mm units. The line equations for the diffracted beam are then

$$X_d/(X_p - X_n) = Y_d/(Y_p - Y_n) = Z_d/(Z_p - Z_n). \tag{16}$$

At the same time, if a flat detector, situated at a distance, D, from the crystal with 2θ swing equal to zero, is used to record the diffraction pattern, the plane equation for the detector is simply

$$X_d = D. \tag{17}$$

Solving this simple set of simultaneous equations (15) to (17) gives the detector coordinates (Y_d, Z_d),

$$Y_d = D[(Y_p - Y_n)/(X_p - X_n)] \tag{18}$$

$$Z_d = D[(Z_p - Z_n)/(X_p - X_n)]. \tag{19}$$

For a detector with non-zero 2θ swing angle, it is most convenient to have a new Cartesian system (x, y, z), which is related to the original Cartesian system by a simple rotation around the 2θ swing axis. Therefore the vector $\mathbf{O_nP}$, or $[(X_p - X_n), (Y_p - Y_n), (Z_p - Z_n)]$ expressed in the new Cartesian system (x, y, z) will be a simple matrix operation, *i.e.*,

$$\begin{bmatrix} (x_p - x_n) \\ (y_p - y_n) \\ (z_p - z_N) \end{bmatrix} = \begin{bmatrix} \cos 2\theta & \sin 2\theta & 0 \\ -\sin 2\theta & \cos 2\theta & 0 \\ 0 & 0 & 1 \end{bmatrix} \begin{bmatrix} (X_p - X_n) \\ (Y_p - Y_n) \\ (Z_p - Z_n) \end{bmatrix}. \tag{20}$$

After this coordinate transformation, the calculation of detector coordinates (y_d, z_d) takes exactly the same form. The calculation of detector coordinates for the diffracted beam O_xP is performed in the same fashion.

3. Features of the diffraction pattern

From the above algorithm, given the crystal space group, cell dimensions and known experimental conditions (*e.g.* source distribution, detector-to-crystal distance and 2θ swing angle), if one knows the crystal orientation, the locations and shapes of the diffraction pattern can be predicted. However, the inverse problem, deriving crystal cell dimensions and orientation parameters from experimental diffraction patterns (commonly known as the indexing problem), is a little more difficult with a convergent beam than indexing still patterns generated by a well collimated beam. The reason is that the uncertainty in coordinates of the source origin contributing to a particular reflection makes it difficult to accurately determine the Cartesian coordinates of the corresponding

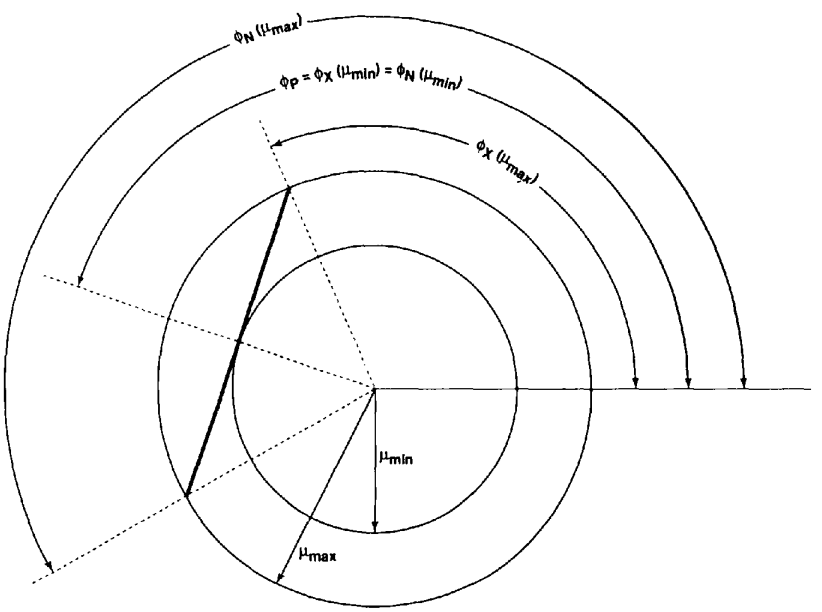

Fig. 3. A φ–μ polar plot of a typical reflection. The dark solid line represents the area contributing to the particular reflection. In this plot $\mu_{max} = 1.00°$, $\mu_{min} = 0.66°$. The plot line is nearly straight. With much larger μ_{max} values, the plots should have noticeable curvature. At μ_{min}, either $\varphi_x = \varphi_n = \varphi_p$ (shown here), or $\varphi_x = \varphi_n = \varphi_p + \pi$.

reciprocal lattice points, which are the key to a successful indexing procedure. This is, in a way, similar to the difficulty in indexing oscillation images, where the oscillation angle at which a particular diffraction occurs is only known with an uncertainty of the oscillation range. A simple solution to this problem is to take one or more still images with a pinhole which restricts the beam divergence. These images are to be used for indexing purpose only. If this method is not available, the situation is still not entirely hopeless. Before going into details of the diffraction vector determination, let us first analyze the shape of a diffraction spot.

3.1. *Reflection spot shape*

It has been pointed out that the trace of a reciprocal lattice point P passing the reflecting sphere at varying μ angles, forms a planar circle in a moving frame. In the laboratory frame, the trace of beam origins also forms a planar circle. These two facts are equivalent. However, it is more convenient to discuss the spot shape in the laboratory frame.

As mentioned previously, for a convergent source, all the beam origins, O_s's, are situated on a sphere centered on O^* with radius of λ^{-1}, and they also lie within a convergent cone with the cone axis coinciding with the X axis. For a reciprocal lattice point P involved in diffraction, the condition that a beam participates in this particular reflection is that the distance from P to the beam origin equals λ^{-1}. For this condition, one can construct another sphere centered on P, again with radius of λ^{-1}. The intersection of this sphere and the sphere element of beam origins is an arc which belongs to a circle on the plane perpendicular to and bisecting vector **O*P** (Fig. 4). The radius of this circle is $[\lambda^{-2} - (\rho/2)^2]^{1/2}$, where ρ is the magnitude of vector **O*P**. Beams with their origins lying on this arc satisfy the diffraction condition, hence contribute to this particular reflection. This explains the conic nature of the spot shape, however, the curvature of the spot becomes noticeable only when the beam divergence is large, *e.g.* 6° or more. In most cases, one sees only tangential elongation of the spots. Hereafter, we will refer to this tangential elongation as the spot length, and the radial width as the spot width.

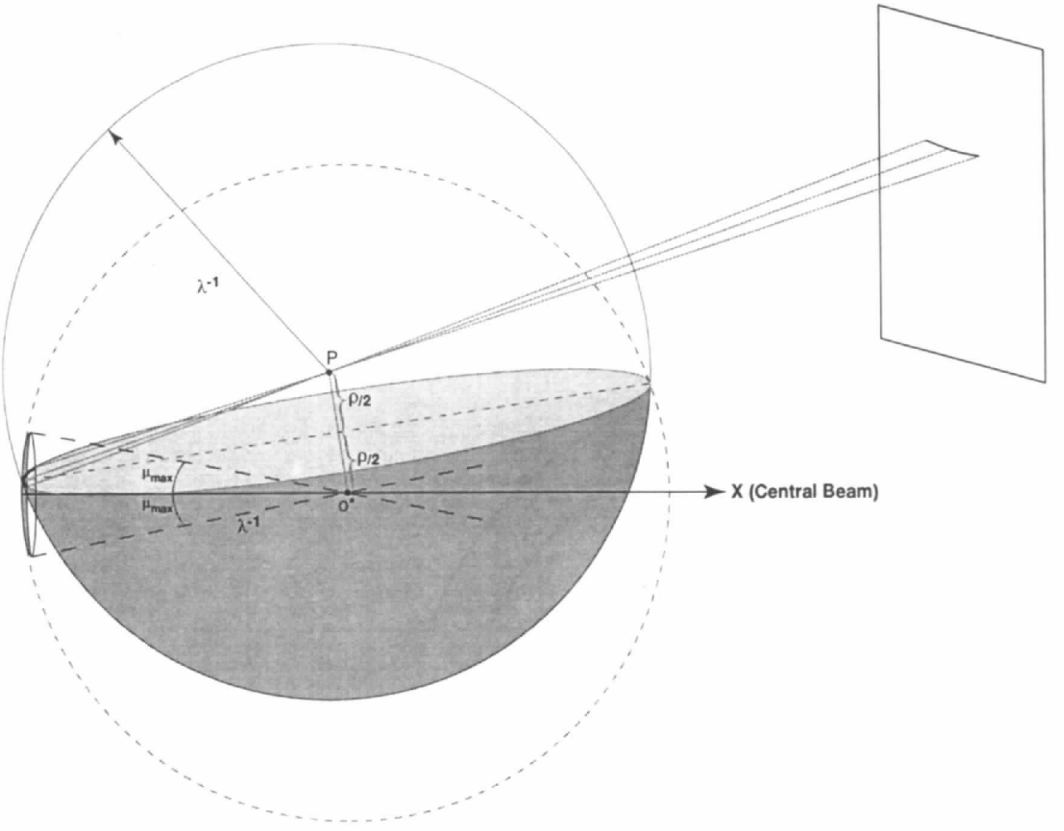

Fig. 4. A three-dimensional schematic diagram of diffraction geometry for a reciprocal lattice point P. Two spheres both with radius of λ^{-1} are shown by circular outlines, one of which centered on P (shown as a solid circle), the other centered on O^* (shown broken circle). Beam origins lie on the latter within the convergent cone of angle μ_{max}. The intersection of the two spheres is a planar circle of radius of $[\lambda^{-2} - (\rho/2)^2]^{1/2}$, which is perpendicular to, and bisecting, the scattering vector **O*P**. The dark line within the convergent cone shows the arc which is part of that planar circle. The angle spun over P by this arc is the angular spread of this particular reflection. The convergence angle μ_{max} is exaggerated.

3.2. *Diffraction vector determination*

For ease of discussion, we will consider only the case with the detector 2θ swing angle at zero. We know that the mid-point of a diffraction spot on the detector with coordinates (Y_d, Z_d) corresponds to a single source origin $\tilde{O}$ at μ_{min}. It is obvious that points $\tilde{O}$, O, O^* and P all line on the same plane defined by the crystal origin (0,0,0), the film center $(D,0,0)$ and the mid-point of the diffraction spot (D,Y_d,Z_d) in three-dimensional space. Thus, in terms of cylindrical coordinates, only φ_p is known for the diffraction vector $\mathbf{O^*P}$, *i.e.* $\varphi_p = \arctan(Z_d/Y_d)$. R_p and X_p still remain undetermined. There is also an angular relationship,

$$\angle\tilde{O}O^*P = \angle OO^*P - \mu_{\tilde{o}} = \beta - \mu_{\tilde{o}}, \qquad (21)$$

where

$$\mu_{\tilde{o}} = (\pm)\mu_{min}, \qquad (22)$$

the plus sign should be chosen when point P and $\tilde{O}$ lie on the same sides of line OO^* in the OO^*P plane; the minus sign should be chosen otherwise (Fig. 2). The uncertainty in the sign and magnitude of $\mu_{\tilde{o}}$ in the above angular relationship is the source of difficulty in accurately determining the Cartesian coordinates of diffraction vector $\mathbf{O^*P}$. An intuitive approach would be to ignore this angle altogether, *i.e.*, let $\angle\tilde{O}O^*P = \beta$, or let $\mu_{\tilde{o}} = (\pm)\mu_{min} = 0$. This would give a maximum error of μ_{min} in beam origin $\tilde{O}$. For a source with beam divergence, μ_{max}, significantly greater than 1°, the error propagating to the direction and magnitude of $\mathbf{O^*P}$ might be too great to provide successful indexing. Nevertheless, for macromolecular crystals, one usually would restrict the beam divergence angle to a maximum of around 1° to avoid serious overlapping, (*cf.* the simulation results shown later). Furthermore, with the knowledge of the relationship between the spot length on the detector and $\mu_{\tilde{o}}$, the situation can be improved by a spot selection process.

The general feature of the relationship is that the angular spread of a diffraction spot tangential length approaches zero at $\mu_{min} = \mu_{max}$, *i.e.* $\mu_{\tilde{o}} = (\pm)\mu_{max}$, and it approaches a maximum value of $2\mu_{max}$, which is the source angular spread, at μ_{min} near zero (detailed derivation of this relationship is given in *Appendix B*). The spot angular spread *versus* $\mu_{\tilde{o}}$ for a typical value of beam divergence $\mu_{max} = 1.25°$ at three different apparent scattering angle α's is tabulated in Table 1 (for definition of apparent scattering angle *cf. Appendix A*). It can be seen that the α value has only a minor effect on this relationship. For any particular spot, the error in letting $\angle\tilde{O}O^*P = \beta$ is $(\pm)\mu_{min}$, which could range from nearly zero for the longest spot lengths to $(\pm)\mu_{max}$ for nearly zero spot lengths. However, if one chooses only those spots with their angular spreads larger than 80% of the source angular spread $2\mu_{max}$, then the maximum error in letting $\angle\tilde{O}O^*P = \beta$ is reduced to around 0.75° from 1.25°. In many cases, this magnitude of error may be tolerable.

Table 1. *Spot angular spread versus $\mu_{\tilde{o}}$ at three different α values*

All numbers in °. Numbers shown are for beam divergence μ_{max} = 1.25°.

$\mu_{\tilde{o}}$	α = 10	α = 30	α = 50
−1.25	0.0000	0.0000	0.0000
−1.24	0.3161	0.3167	0.3170
−1.23	0.4460	0.4466	0.4474
−1.22	0.5450	0.5458	0.5472
−1.21	0.6281	0.6290	0.6303
−1.20	0.7006	0.7019	0.7036
−1.15	0.9806	0.9823	0.9843
−1.10	1.1884	1.1905	1.1924
−1.05	1.3575	1.3597	1.3621
−1.00	1.5011	1.5034	1.5060
−0.95	1.6260	1.6283	1.6309
−0.90	1.7361	1.7385	1.7413
−0.85	1.8341	1.8365	1.8393
−0.80	1.9220	1.9244	1.9270
−0.70	2.0722	2.0745	2.0770
−0.60	2.1940	2.1921	2.1982
−0.50	2.2920	2.2938	2.2957
−0.40	2.3691	2.3706	2.3722
−0.30	2.4273	2.4284	2.4296
−0.20	2.4680	2.488	2.4695
−0.10	2.4920	2.4924	2.4929
0.00	2.4998	2.4998	2.4998
0.10	2.4916	2.4912	2.4908
0.20	2.4672	2.4665	2.4656
0.30	2.4262	2.4256	2.4236
0.40	2.3676	2.3661	2.3645
0.50	2.2902	2.2885	2.2864
0.60	2.1920	2.1899	2.1876
0.70	2.0700	2.0677	2.0652
0.80	1.9196	1.9172	1.9146
0.85	1.8317	1.8292	1.8265
0.90	1.7336	1.7312	1.7283
0.95	1.6235	1.6212	1.6183
1.00	1.4988	1.4964	1.4938
1.05	1.3553	1.3531	1.3506
1.10	1.1863	1.1844	1.1818
1.15	0.9789	0.9771	0.9751
1.20	0.6993	0.6980	0.6970
1.21	0.6267	0.6256	0.6244
1.22	0.5439	0.5429	0.5416
1.23	0.4448	0.4440	0.4427
1.24	0.3151	0.3149	0.3140
1.25	0.0000	0.0000	0.0000

Spots with the angular spreads larger than the source angular spread are overlapped and should be discarded. Because a convergent beam brings several times more diffraction spots onto the area detector than does a well collimated beam, there will still be a sufficient number of spots to be used for indexing. For individual spots, their corresponding μ_{min} (or magnitude of $\mu_{\tilde{o}}$) values can be roughly estimated according to their angular widths through calculations similar to that of Table 1. At the initial stage of a least-squares procedure, appropriate weights can be assigned to individual reciprocal vectors according to their uncertainties, *i.e.*, μ_{min}. Prior to final least-squares refinement, the signs of $\mu_{\tilde{o}}$ could be determined, even for those spots with narrower angular

spreads, thus allowing for a more accurate determination of orientation and detector parameters. In the final refinement, information on observed spot lengths could also be included.

3.3. *Overlapping reflections*

With knowledge of the diffraction spot shapes, a practical two-step procedure to test for overlap between reflections can be set up. In the first step, for each reflection, the detector coordinates at the two ends of a spot are calculated, which correspond to diffraction at μ_{max}; and then, a rectangle for each spot is defined by the two extreme detector coordinates which contains an additional damping area allowing for spot broadening. Two spots are considered separated when the corresponding rectangles do not overlap. This method allows rapid initial screening for possible overlap.

Owing to the tangential elongation, spots failing the above test can still be separated and are further tested in the second slightly more computationally intensive step, which calculates the minimum distance between two spots. For the detector at swing zero. *i.e.*, $2\theta = 0$, each spot can also be expressed in polar coordinates with the origin at where the central direct beam intercepts the detector plane (in this case, the detector center).

Thus,

$$Y_i = r_i \cos\varphi_i$$
$$Z_i = r_i \sin\varphi_i,$$

where, to a good approximation, r_i can be considered as constant within the spot, while φ_i varies from $\varphi_{i,min}$ to $\varphi_{i,max}$. Then, the distance between two points on two different diffraction spots is

$$d = (r_i^2 + r_j^2 - 2r_i r_j \cos\Delta\varphi_{ij})^{1/2}. \tag{23}$$

The minimum distance occurs at the minimum value for $\Delta\varphi_{ij}$. When the two angular ranges, $(\varphi_{i,min}, \varphi_{i,max})$ and $(\varphi_{j,min}, \varphi_{j,max})$, overlap each other, then $(\Delta\varphi_{ij})_{min} = 0$, hence, $d_{min} = |r_i - r_j|$. Two spots are considered separated when the minimum distance, d_{min}, is greater than a set value dictated by the spot broadening effects.

In order to be able to measure the experimental integrated intensities by a profile-fitting procedure, and to separate spots which fail the first test but pass the second test, it is suggested that intensity profiles be expressed in polar coordinate boxes, in which Δr maintains more or less constant with a narrow r range in a sector of the film, while $r\Delta\varphi$ should be adjustable according to the predicted spot tangential length. Intensity profiles expressed this way follow more closely to the natural spot shapes.

4. Source distribution and diffraction intensities

In any diffraction data collection method, an important factor is to bring all the reflections recorded at different geometrical conditions onto the same scale. The polarization factor here is the same as in conventional methods, assuming a circular polarization. The Lorentz factor in moving crystal methods, which addresses the different time factors for different reflections does not exist here. In its place, there is a factor which addresses the fact that individual reflections have their unique parts of the source contributing to diffraction. It is, therefore, necessary to introduce an effective source coverage factor, or simply source factor.

4.1. *Effective source coverage factor*

From Fig. 3, one immediately realizes that the part of the source contributing to one particular reflection is that along the φ–μ curve. Hence, the effective source coverage factor, L, can be expressed as the following line integral,

$$L = \int_{\mu_{min}}^{\mu_{max}} \{[S(\mu, \varphi_n) + S(\mu, \varphi_x)] \times [1 + (\mu\varphi_n')^2]^{1/2} / \sin 2\theta\}\, d\mu, \tag{24}$$

where we have recognized that $\varphi_n' = d\varphi_n(\mu)/d\mu = -\varphi_x'$; $S(\mu,\varphi)$ is the source angular intensity distribution function. Less obvious is the factor $(1/\sin2\theta)$ in the line integral. When the source origin O_s deviates from the φ–μ curve laterally by a unit, the magnitude of O_sP deviates from λ^{-1} by $\sin2\theta$ (in Fig. 4, the two sphere surfaces making an constant angle of 2θ to each other at intersection), therefore, the corresponding recorded intensity is inversely proportional to $\sin2\theta$. This is similar to the derivation of Lorentz factor in moving crystal methods, where the Lorentz factor is inversely proportional to the rate of a reciprocal lattice point passing the reflecting sphere. The derivative φ_n' or φ_x' are analytical but somewhat complicated functions. In an actual calculation, one would prefer a simpler numerical form, *i.e.*,

$$L = \sum S(\mu, \varphi)\{(\mu\Delta\varphi)^2 + (\Delta\mu)^2\}^{1/2}/(\sin 2\theta), \tag{25}$$

where the summation is over the entire length of the φ–μ curve.

4.2. *Source angular intensity distribution*

The source angular intensity distribution function, or source distribution, $S(\mu,\varphi)$ can be determined experimentally by an area detector at a long distance from the focal point. Rigorously speaking, the recorded intensity distribution of the direct beam is a convolution of the (angular) source distribution with the two-dimensional lateral intensity distribution at the focal point. The longer the distance, the smaller the convolution effect caused by the finite size of the focal spot, and the higher the angular resolution. The recorded values can either be used to calibrate the characteristic parameters of a model function, or be used directly in the calculation of the source

factor, which will make the estimates more accurate at a higher computation cost.

In cases that the source distribution can be approximated by a radial function $S(\mu)$, *i.e.*, it possesses rotational symmetry, additional saving in computation ensues. One could tabulate the source factor L against a series of μ_{min}'s beforehand, the source-factor value for any particular reflection is evaluated by interpolation according to its μ_{min} value.

An ideal source distribution is one which shows small variation for convergence angle $\mu < \mu_{max}$ and which diminishes abruptly to zero beyond μ_{max}. This requirement can be achieved only with perfect optics (with no optical aberration). The optical aberration for an X-ray polycapillary lens is much higher than that for conventional optical lenses. One can only try to minimize the gap between $\mu_{0.33}$ (where source distribution, S, is at one third of its peak value) and $\mu_{0.01}$ (where S diminishes, in practice). Here, the numbers 0.33 and 0.01 are chosen somewhat arbitrarily. Reflections with their μ_{min} values falling within this 'tail' of the source distribution curve, are more weakly exposed (corresponding to a small source factor), therefore, are generally less accurately measured. The tail of a Gaussian curve is fairly long (ranging approximately from 1.5σ to 3.0σ), therefore, it is far from ideal. The length of the tail can be shortened either by reducing optical aberration of the lens, and/or by improving collimation.

4.3. *Understanding crystal movement*

The effects of beam convergence/divergence on still diffraction patterns have been analyzed. This gives us a new perspective on moving crystal methods. Let us consider first the case of an oscillating crystal with narrow mosaicity. For a reciprocal lattice point involved in diffraction before the crystal movement, a rotation around ω (collinear with Z, *i.e.*, normal beam condition) axis will cause its associated φ–μ curve to shift (changing μ_{min} accompanied by small change in φ_p), or even to sweep out of the range of the sphere element of origins. At the same time, the movement may also bring some reciprocal lattice points, not involved in diffraction before the movement, into diffracting condition, or even sweeping through the entire range of the sphere element of origins. For the last case, a spot's tangential length varies from zero to a maximum value corresponding to the total source angular spread, and then back to zero again. Thus, the spot is nearly isotropic in dimensions and is considered 'full' by crystal scan in the sense that all parts of the source have been brought to diffraction condition for this particular reflection. Otherwise, diffraction spots are considered 'partial'. The estimate of partiality for each recorded reflection is important for bringing them onto the same scale.

Certain reflections with their φ_p values close to $\pi/2$ or $3\pi/2$, ω scans bring mostly tangential movement of the φ–μ curves. The reflections are brought in and out of diffraction conditions by the ω scans, while their φ–μ curve movements are localized in a small region of the source. Only part of the source contributes to these reflections, therefore, they cannot be scaled properly and have to be discarded from the data set. In the case of a highly collimated beam with mosaic crystal, this effect of beam convergence is negligible. However, in the case of a more perfect crystal exposed to a more convergent beam, *e.g.*, from highly convergent double mirrors, attention should be taken to discard the reflections recorded with their φ_p's close to $\pi/2$ or $3\pi/2$. Fortunately, many of these recorded reflections are discarded by conventional data processing software for other reasons, such as Lorentz factors outside allowable range, total or partial blockage by the beam stop, or in the region of detector shaded by the crystal mounting capillary. For reflections with multiple observations, they may also be among those rejected for unexplained (purely statistical) reasons.

5. Simulation and preliminary experimental results

5.1. *Diffraction pattern*

Experimental diffraction patterns using a polycapillary optic (a prototype manufactured by XOS, Inc.) were taken for lysozyme crystal (chicken egg white, tetragonal form with cell dimensions $a = b = 79.3$, $c = 37.9$ Å), at an arbitrary orientation. The beam convergence of the optic output is approximately 0.98° (full width at half maximum, FWHM). It was collimated by a modified 0.5 mm collimator with its back pinhole expanded to allow more convergent beams to pass through. The beam thus collimated was roughly approximated by a radial Gaussian with $1\sigma = 0.133°$. Two different crystal-to-detector distances were used and the pattern recorded on an R-AXIS II imaging-plate detector (Figs. 5*a* and 6*a*). A Rigaku RU-300 Cu $K\alpha$ rotating-anode generator operating at 38 kV, 70 mA was used as the X-ray source with 1.5 min exposures. The MSC *Biotex* software was used to provide an orientation matrix for the crystal. Using the algorithms described previously, simulated diffraction patterns were also generated (Figs. 5*b* and 6*b*), with our developmental software. The orientation and conditions are the same as their experimental counterparts. In addition to the tangential elongation described previously, the software takes into account other diffraction spot broadening factors, such as beam focus spot size (crystal volume irradiated by the beam), and the mosaic spread of the crystal. The combining effect of these two factors is assumed to be a convolution of a Gaussian distribution function with a simple geometry form function. All calculations terminated at approximately 1% of peak values, thus μ_{max} was set at $3\sigma = 0.40°$ (where the Gaussian curve reaches 1.1% of its peak value). Beam aberration, absorption, misfocusing and spectral dispersion effects are ignored. Except for the diffuse scattering background

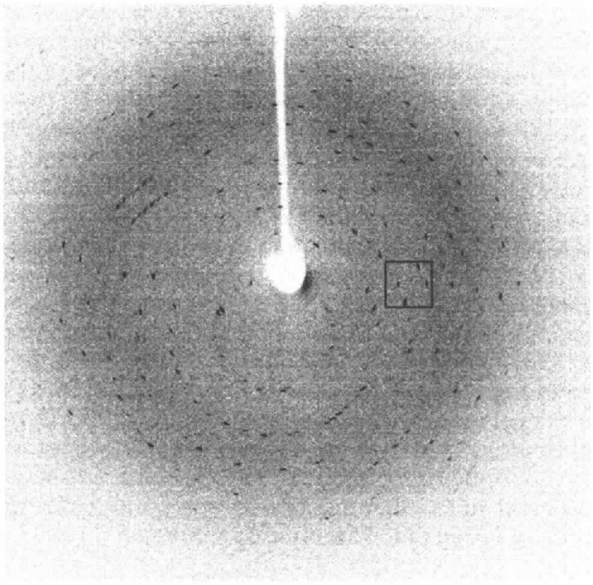

(*a*)

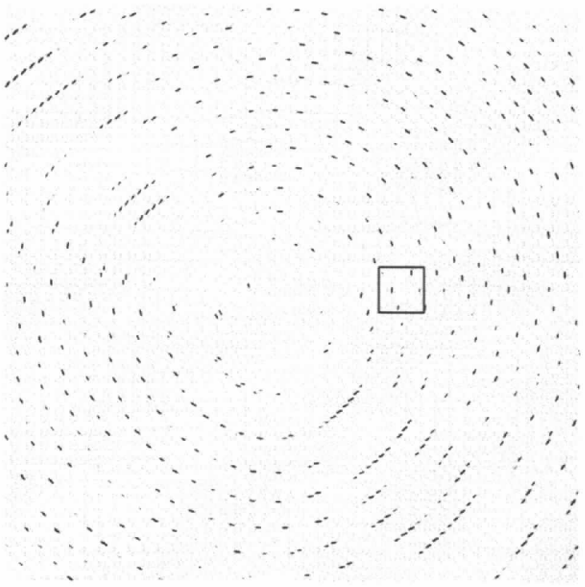

(*b*)

Fig. 5. (*a*) Experimental diffraction pattern of a tetragonal chicken egg-white lysozyme crystal. A polycapillary lens was used on Rigaku RU-300 generator, running at 38 kV and 70 mA, exposure time 1.5 min. Output beams from the polycapillary lens were collimated by a modified 0.5 mm collimator (see the main text), resulting a beam with approximate focus spot size of 0.36 mm diameter and 0.40° maximum divergence (3σ of a Gaussian). Ni (12.5 μm) and Al (25 μm) filters were used to eliminate residual white and Cu $K\beta$ radiation. The pattern was recorded by an R-AXIS II imaging plate with crystal-to-detector distance 130 mm; (*b*) Simulated diffraction pattern of the same crystal at the same orientation. Focus spot size, divergence angle and crystal-to-detector distance are the same as in (*a*). A mosaic spread of 0.01° (1σ of Gaussian) was used.

(not modeled), there is striking agreement between experiment and simulation.

Close examination of the diffraction spots at different distances showed that the farther the crystal-to-detector distance, the larger the aspect ratio of spot length over its radial width (Figs. 7*a* and 7*b*). This fact indicates that the spot broadening is caused mainly by the size of focus spot of the optical lens, rather than by the mosaicity of the crystal. Unlike tangential elongation and mosaic

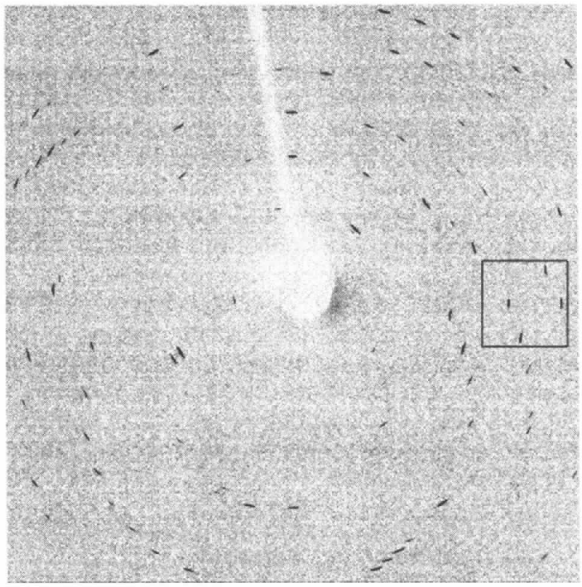

(*a*)

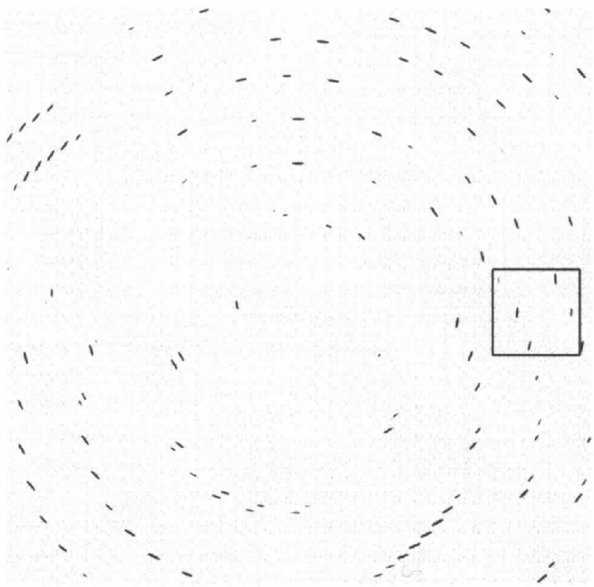

(*b*)

Fig. 6. (*a*), (*b*) Same as Figs. 5(*a*) and 5(*b*), respectively, except the crystal-to-detector distance is at 260 nm.

spread, which produce spot broadening proportional to the crystal-to-detector distance, finite size of focus spot produces constant spot broadening over the distances. In the above experiment, the beam was collimated to 0.36 mm diameter at the crystal. The simulated patterns (Figs. 5*b* and 6*b*) were generated using this spot size and a mosaic spread value of 0.01° (1σ of a Gaussian distribution function). Detailed features of the same set of spots are shown in Figs. 7(*c*) and 7(*d*), which agree well with experiment.

It should be pointed out that the mosaic spread used in the simulation is at least an order of magnitude smaller than that commonly found with conventional macromolecular data-processing software packages. In fact, macromolecular crystals usually have narrow mosaic spreads, and careful rocking curve measurements on several different protein crystals indicated they amount to around 0.004–0.030° (1σ of a Gaussian converted from the FWHM, *i.e.*, FWHM = 2.3σ, Colapietro *et al.*, 1992; Snell *et al.*, 1995, 1997). The large mosaicity used with conventional data-processing software is actually a parameter to deal with a combination of many different physical phenomena, such as beam divergence, spectral dispersion, crystal size, *etc.*

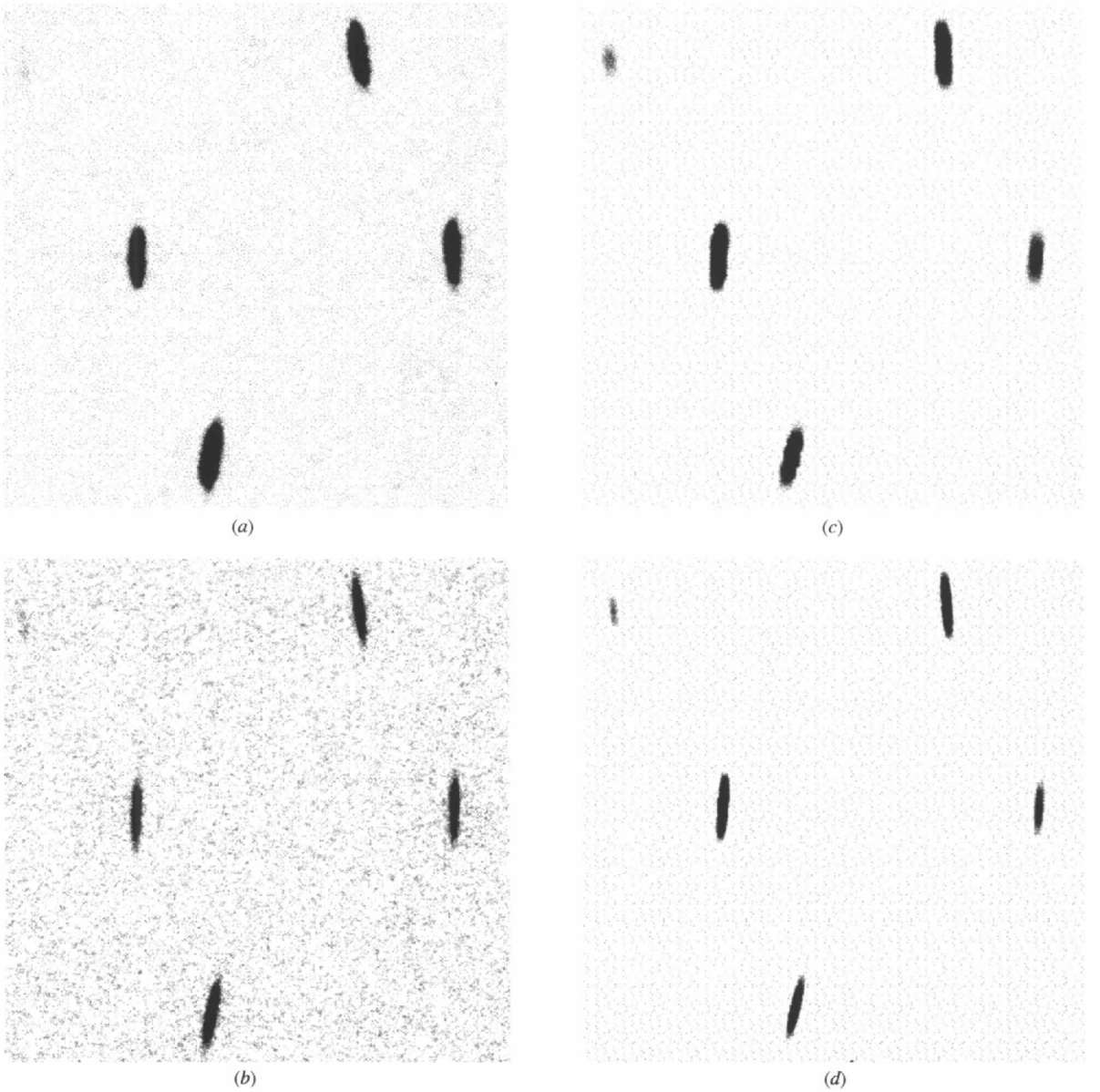

Fig. 7. (*a*) Enlargement of an area of experimental pattern as marked in Fig. 5(*a*) (with crystal-to-detector distances D = 130 mm); (*b*) same as marked in Fig. 6(*a*) (D = 260 mm); (*e*) enlargement of an area of simulated pattern as marked in Fig. 5(*b*) (D = 130 mm); (*d*) same as marked in Fig. 6(*b*) (D = 260 mm). These figures cover diffractions within the same solid angle. The magnifications used are proportional to D.

The effect of beam divergence can be seen by comparing Figs. 5(*b*), 8(*a*) and 8(*b*) (with convergence angles of 0.40, 1.00 and 2.00°, respectively). It is easy to understand that the wider the beam divergence the more serious the overlapping effect. This is in much the same way as in oscillation or screenless precession methods, where wider oscillation/precession angles result in more pronounced overlapping effects. A unique feature of the convergent beam method is that the overlapping effect is most serious when the crystal is oriented near low index zone axes (Fig. 9), even more so with crystals of higher symmetry. This is owing to the fact that at these orientations, there are more reciprocal vectors with equal (or nearly equal) magnitudes involved in diffraction. Their diffraction spots all line on a circle with equal (or nearly equal) scattering angle. The tangential elongation effect of a divergent beam causes these spots to connect and/or overlap, hence merging into long arcs of a circle, or even a closed circle. It is therefore necessary to avoid collecting data close to low index axial orientations.

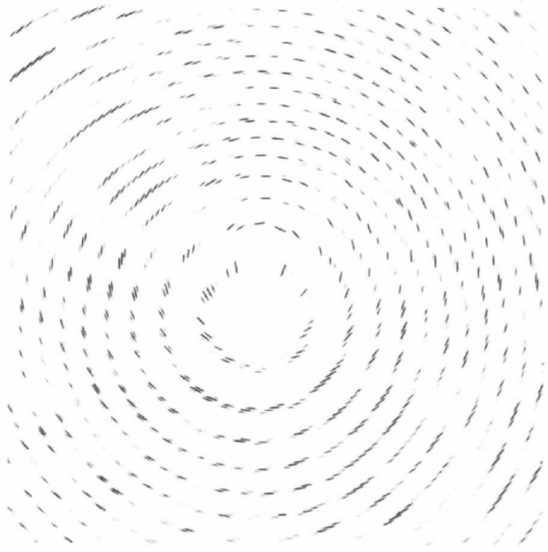

(*a*)

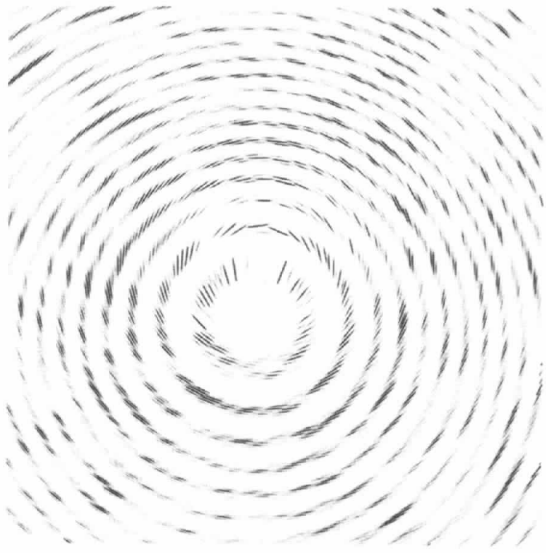

(*b*)

Fig. 8. Simulated patterns generated with the same conditions as in Fig. 5(*b*) except that different maximum beam divergence angles were used. (*a*) $\mu_{max} = 1.00°$, overlapping is more serious than Fig. 5(*b*), however, majority of the spots still can be separated; (*b*) $\mu_{max} = 2.00°$, overlapping is very serious. Source distributions are all assumed to be radial Gaussian truncated at 3σ.

5.2. *Simulated data collection*

Another type of simulation has also been carried out, which calculates the data coverage of a series of still diffraction pictures for a lysozyme crystal with the same missetting angles as those for the experimental conditions in Fig. 5(*a*). The crystal-to-detector distance was set at 10 cm; the mosaic spread at 0.01°, beam focus spot size at 0.36 mm diameter; the beam source profile was assumed as a radial Gaussian distribution function truncated at 3σ. The successive exposures were taken at an increment of 2.0° with a beam divergence of 1.0° (total source angular spread 2.0°). The results of this simulation are tabulated in Table 2. The overlapping effect is not a problem for a majority of the exposures, except at the beginning of the series of exposures, which is close to a low index zone axis. Over 93% of a complete data set, up to 2.0 Å resolution, can be collected with only 20 still images.

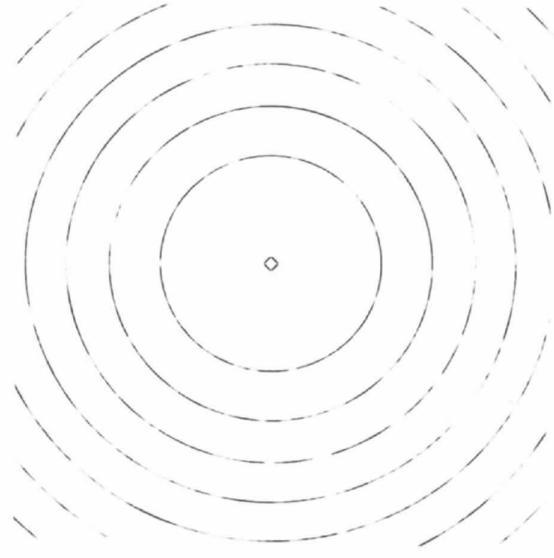

Fig. 9. Simulated pattern generated with the same conditions as in Fig. 8(*a*) except that the crystal is reoriented with (0,0,1) direction along *X* axis. The serious overlapping effect at low index zone axes is the characteristics of the divergent beam and high symmetry of the crystal. Because of serious overlap, it seems that the spots are curved inward, though they are actually elongated tangentially (strictly speaking, they are conic and curved outward).

Table 2. *Data coverage of a simulated data-collection run for a tetragonal chicken egg-white lysozyme crystal*

The crystal was assumed mounted with the same missetting angles (−43.57, 7.96, 1.12°) as those of the conditions in Fig. 5(*a*). The crystal-to-detector distance is set at 10 cm; mosaic spread at 0.01°, beam focus spot size at 0.36 mm diameter; source distribution is assumed as a radial Gaussian distribution function truncated at 3σ. The successive exposures are taken at an increment of 2.0° with a beam divergence of 1.0° (total source angular spread 2.0°).

(*a*) Data coverage for individual still images

ω†	Observations	Rej1	Rej2	Rej3	Independent	(% Shell)	Summed	(% Cumul)
5.0	2053	30	61	672	1180	17.4	1180	13.8
7.0	2048	26	115	665	335	3.7	1515	17.7
9.0	2106	26	59	677	657	7.2	2172	25.3
11.0	2046	27	0	655	668	8.4	2840	33.1
13.0	2050	31	0	627	640	8.8	3480	40.6
15.0	2068	28	0	662	600	7.8	4080	47.6
17.0	2074	29	0	691	520	6.6	4600	53.7
19.0	2069	25	0	692	453	5.4	5053	59.0
21.0	2074	24	0	649	419	4.4	5472	63.9
23.0	2040	30	0	656	337	3.3	5809	67.8
25.0	2077	28	0	658	280	3.1	6089	71.1
27.0	2101	29	0	668	290	3.1	6379	74.4
29.0	2057	27	0	651	261	2.9	6640	77.5
31.0	2050	25	0	659	234	2.8	6874	80.2
33.0	2055	29	0	639	231	2.5	7105	82.9
35.0	2061	27	0	652	220	2.2	7325	85.5
37.0	2053	27	0	657	205	2.1	7530	87.9
39.0	2060	29	0	645	180	1.9	7710	90.0
41.0	2089	27	0	679	157	1.7	7867	91.8
43.0	2059	29	841	368	128	1.8	7995	93.3
Total	41290	553	1076	12922	N/A	N/A	7995	93.3

(*b*) Resolution breakdown of data coverage

D_{min}†	Observations	Rej1	Rej2	Rej3	Independent	(% Shell)	Summed	(% Cumul)
5.43	2123	0	15	693	432	88.2	432	88.2
4.31	2166	0	11	741	435	96.2	867	92.0
3.76	2109	0	14	695	429	97.5	1296	93.8
3.42	2104	0	7	716	423	95.7	1719	94.2
3.17	2113	0	8	698	411	95.8	2130	94.5
2.99	2161	0	14	725	417	95.6	2547	94.7
2.84	2082	0	39	680	409	96.2	2956	94.9
2.71	2047	0	65	636	397	94.3	3353	94.9
2.61	2074	0	75	611	416	96.3	3769	95.0
2.52	2019	0	82	577	399	95.2	4168	95.0
2.44	2112	0	98	631	398	93.6	4566	94.9
2.37	1965	0	63	590	396	95.2	4962	94.9
2.31	2102	0	76	646	400	93.9	5362	94.9
2.25	1917	0	79	603	381	93.8	5743	94.8
2.20	2137	0	83	681	401	93.3	6144	94.7
2.15	2031	0	79	661	384	92.3	6528	94.5
2.11	1983	0	73	612	379	91.8	6907	94.4
2.07	2079	32	71	647	386	90.8	7293	94.2
2.03	1989	174	68	542	364	88.3	7657	93.9
2.00	1977	347	56	537	338	81.6	7995	93.3
Total	41290	553	1076	12922	N/A	N/A	7995	93.3

† Rej1, reflections too close to the edge of (or completely off) the detector; Rej2, reflections overlapped; Rej3, reflections with source factors less than 30% of averaged values; ω in °, D_{min} in Å.

Reflections with very small effective source coverage factors cannot be measured accurately. These reflections correspond to reciprocal lattice points too close to the limiting surface of the region of the reciprocal space that is stimulated by the beam. *i.e.* the μ_{min} values of these reflections are very close to the maximum convergence angle μ_{max} of the beam. A rejection criterion has been applied such that reflection spots with their effective source coverage factor less than 30% of the average value of the entire detector frame are rejected. This is equivalent to a criterion based on a set upper limit for μ_{min} to be accepted. Using this criterion, a fair amount of data is rejected. This is because a Gaussian, truncated at 3σ, is assumed for the source distribution, which has a long tail. With reduced lens optical aberration and better collimation this situation can be improved.

6. Discussion

We have so far established the general features and the interpretation of diffraction patterns of a stationary crystal from a convergent source. Simulations were carried out for a macromolecular crystal (tetragonal, chicken egg-white lysozyme), which showed that with a convergence angle (in this case, total source angular spread around 2.0°), diffraction spots can be separated and interpreted. For crystals with longer unit-cell axes narrower source angular spread should be used. At this beam divergence range, the intensity on the crystal integrated over the entire convergence angle is many times of that of a highly collimated beam from the same X-ray source. This should generally speed up the data collection by as many folds. In order to be able to fully utilize the beam while keeping diffraction spots separated the beam divergence should be made adjustable, *e.g.*, by using a changeable pin-hole device with a series of different sizes of diameters. With this device, an optimal beam divergence angle can be selected according to the particular crystal system to be studied.

An important factor which has a profound effect on spot spread and overlap is beam focus spot size. The simulation was carried out with beam focus spot size of 0.36 mm diameter. It is now technically possible to achieve a beam focus spot size of 0.1 mm diameter, and in the future perhaps even less. Just as in the conventional rotation (oscillation) method, where a wider ω scan brings in more reflections into reflection with a lower signal/background ratio, a wider source angular spread brings in more reflections into diffraction but at a price of lowered signal/background ratio. As for the data coverage, this method is very similar to that of a screenless procession method, which has the advantage of a smaller 'blind' cusp region of the reciprocal space as compared with the oscillation method, and the disadvantage of not being able to explore the reciprocal space in a more systematic way for successive exposures with one rotation axis.

Because of serious overlap of diffraction spots at orientations close to low index zone axes, a goniostat with two or more axes designated for orienting the crystal can ease the process of reaching desired orientations for exposure. Rotating the crystal around a single goniostat axis between exposures usually results in the collection of many reflections (or their symmetry mates) repeatedly. The most efficient way to collect a 'complete' data set is to find out the minimum number of exposures required and their corresponding crystal orientations beforehand. Due to the huge number of possible crystal orientations, and particularly due to the combinatorial nature of calculation, this is a prohibitive task. Nikonov & Chirgadze (1985) proposed probably the next best thing – a procedure of determining an 'optimum sequence' of exposures, in which the optimization is done only at each step of the sequence for maximum efficiency. Implementation of this procedure for the current method is under way, which takes into account the Laue group symmetry of the crystal, overlap effect, low source factor rejection and goniostat movement limitations. More importantly, efforts are under way to develop computer programs for indexing, integration and scaling of the recorded images. This will allow a more thorough comparison of the data acquired by the proposed method against those by conventional methods.

The use of a convergent beam with a stationary crystal allows simultaneous data collection over the range of the convergence angle. This decreases the exposure time required to give a complete data set when compared with the conventional oscillation/rotation method. Our analysis shows that interpretation of the resulting diffraction patterns is possible and that this technique could have important application in macromolecular X-ray crystallography. It may also be important for other diffraction applications such as microdiffraction, strain and texture measurements in thin films, *etc.* Such application will be described in other publications.

APPENDIX *A*

Derivation of diffraction condition for source origins

As shown in the main text, [(11)], that for reciprocal lattice point P the diffraction condition for the source points is

$$(X_s - X_p)^2 + (Y_s - Y_p)^2 + (Z_s - Z_p)^2 = \lambda^{-2}, \qquad (26)$$

where coordinates with subscripts s are for those of source origins O_s, which lie on the conic shell with convergent angle μ, while those with subscripts p for reciprocal lattice point P. By inserting the cylindrical coordinate expressions [*cf.* (9)], one has

$$\begin{aligned}\lambda^{-2} &= (X_p + \lambda^{-1}\cos\mu)^2 \\ &\quad + (R_p\cos\varphi_p - \lambda^{-1}\sin\mu\cos\varphi_s)^2 \\ &\quad + (R_p\sin\varphi_p - \lambda^{-1}\sin\mu\sin\varphi_s)^2 \\ &= X_p^2 + \lambda^{-2}\cos^2\mu + 2X_p\lambda^{-1}\cos\mu \\ &\quad + R_p^2\cos^2\varphi_p + \lambda^{-2}\sin^2\mu\cos^2\varphi_s \\ &\quad - 2\,R_p\cos\varphi_p\lambda^{-1}\sin\mu\cos\varphi_s \\ &\quad + R_p^2\sin^2\varphi_p + \lambda^{-2}\sin^2\mu\sin^2\varphi_s \\ &\quad - 2R_p\sin\varphi_p\lambda^{-1}\sin\mu\sin\varphi_s. \end{aligned} \qquad (27)$$

Recognizing that

$$X_p^2 + R_p^2\cos^2\varphi_p + R_p^2\sin^2\varphi_p = \rho^2$$

$$\cos^2\mu + \sin^2\mu\cos^2\varphi_s + \sin^2\mu\sin^2\varphi_s = 1$$

$$\cos\varphi_p\cos\varphi_s + \sin\varphi_p\sin\varphi_s = \cos(\varphi_p - \varphi_s),$$

then we have (11),

$$\cos(\varphi_p - \varphi_s) = (\rho^2 + 2X_p\lambda^{-1}\cos\mu)/(2R_p\lambda^{-1}\sin\mu). \tag{28}$$

The value of a cosine function varies from -1 to $+1$. Therefore, for a solution of the above equation to exist, the following conditions should be satisfied,

$$-1 \le (\rho^2 + 2X_p\lambda^{-1}\cos\mu)/(2R_p\lambda^{-1}\sin\mu) \le 1, \tag{29}$$

or

$$-2R_p\lambda^{-1}\sin\mu < \rho^2 + 2X_p\lambda^{-1}\cos\mu < 2R_p\lambda^{-1}\sin\mu. \tag{30}$$

Rearranging gives

$$\begin{aligned} &-(X_p/\rho)\cos\mu - (R_p/\rho)\sin\mu \le \rho\lambda/2 \\ &\le -(X_p/\rho)\cos\mu + (R_p/\rho)\sin\mu. \end{aligned} \tag{31}$$

Recognizing that $-X_p/\rho = \cos\beta$ and $R_p/\rho = \sin\beta$ we have

$$\begin{aligned} \cos\beta\cos\mu - \sin\beta\sin\mu &\le \rho\lambda/2 \\ &\le \cos\beta\cos\mu + \sin\beta\sin\mu \end{aligned}$$

or,

$$\cos(\beta + \mu) \le \rho\lambda/2 \le \cos(\beta - \mu). \tag{32}$$

Re-casting in angular form leads to

$$-\mu \le \arccos(\rho\lambda/2) - \beta \le \mu, \tag{33}$$

or simply

$$\mu \ge |\arccos(\rho\lambda/2) - \beta|. \tag{34}$$

Hence, we have (12),

$$\mu_{\min} = |\arccos(\rho\lambda/2) - \beta|. \tag{35}$$

APPENDIX *B*

Relationship between angular spot spread and $\mu_{\tilde{o}}$

For an area detector at distance D from the crystal with 2θ swing angle zero, and a spot with its midpoint coordinate of (Y_d, Z_d), let the apparent scattering angle α be the angle between the scattered beam and the central direct beam (note not the same as the beam responsible for diffraction), thus,

$$\alpha = \arctan[(Y_d^2 + Z_d^2)^{1/2}/D]. \tag{36}$$

The midpoint of the detector spot (corresponding to $\mu = \mu_{\min}$) also gives the φ_p angle of the diffraction vector **O*P**,

$$\varphi_p = \arctan(Z_d/Y_d). \tag{37}$$

However, the corresponding source origin $\tilde{O}$ remains uncertain. If we denote $\mu_{\tilde{o}}$ such that,

$$\mu_{\tilde{o}} = (\pm)\mu_{\min}$$

$$X_{\tilde{o}} = -\lambda^{-1}\cos\mu_{\tilde{o}} \tag{38}$$

$$R_{\tilde{o}} = \lambda^{-1}\sin\mu_{\tilde{o}}, \tag{39}$$

where coordinates with subscript $\tilde{O}$ are for the beam origin $\tilde{O}$ responsible for diffraction at $\mu_{\min}$, and here $R_{\tilde{o}}$ carries a sign with $\sin\mu_{\tilde{o}}$, dependent on whether or not $\tilde{O}$ is on the same side with P of OO^* line in the plane defined by OO^*P. From the apparent scattering angle α measured by the mid-point spot detector coordinates, which gives the direction of $\tilde{O}P$, and knowing the magnitude $|\tilde{O}P| = \lambda^{-1}$, we have

$$X_p = \lambda^{-1}(\cos\alpha - \cos\mu_{\tilde{o}}) \tag{40}$$

$$R_p = \lambda^{-1}(\sin\alpha + \sin\mu_{\tilde{o}}) \tag{41}$$

and obviously,

$$Y_p = \lambda^{-1}(\sin\alpha + \sin\mu_{\tilde{o}})\cos\varphi_p \tag{42}$$

$$Z_p = \lambda^{-1}(\sin\alpha + \sin\mu_{\tilde{o}})\sin\varphi_p. \tag{43}$$

On the right-hand sides of the above expressions (40–43) for reciprocal lattice point P, only $\mu_{\tilde{o}}$ is unknown. Now, if Δ is the tangential length of the detector spot, and δ the separation of O_n and O_x at $\mu_{\max}$, from the relationship for similar triangles, we have the angular spread of the spot length,

$$A = \delta/\lambda^{-1} = \Delta/(D^2 + Y_d^2 + Z_d^2 + \Delta^2/4)^{1/2}$$

or,

$$\delta^2/\lambda^{-2} = \Delta^2/(D^2 + Y_d^2 + Z_d^2 + \Delta^2/4) = A^2, \tag{44}$$

where we have recognized that $|O_nP| = |O_xP| = \lambda^{-1}$. On the other hand, δ can be expressed as a function of $\mu_{\tilde{o}}$ as shown below.

We know that at $\mu = \mu_{\max}$ the following relationship exists,

$$\delta = 2\lambda^{-1}\sin\mu_{\max}|\sin(\varphi_n - \varphi_p)|_{\mu_{\max}}|,$$

where the sign $|_{\mu_{\max}}$ means evaluated at $\mu_{\max}$. Or,

$$\delta^2/\lambda^{-2} = 4\sin^2\mu_{\max}[1 - \cos^2(\varphi_n - \varphi_p)|_{\mu_{\max}}]. \tag{45}$$

Inserting expression (11) [same as (28)] for $\cos(\varphi_n - \varphi_p)$ leads to

$$\begin{aligned} \delta^2/\lambda^{-2} = A^2 &= 4\sin^2\mu_{\max}[1 - \cos^2(\varphi_n - \varphi_p)|_{\mu_{\max}}] \\ &= \lambda^2[4\lambda^{-2}\sin^2\mu_{\max} - R_p^2 - X_p^4/R_p^2 \\ &\quad - 4X_p^2\lambda^{-2}\cos^2\mu_{\max}/R_p^2 - 2X_p^2 \\ &\quad - 4X_p\lambda^{-1}\cos\mu_{\max} - 4X_p^3\lambda^{-1}\cos\mu_{\max}/R_p^2]. \end{aligned} \tag{46}$$

Inserting expressions (40) and (41) for X_p and R_p leads to

$$\begin{aligned} &A^2(\sin\alpha+\sin\mu_{\tilde{o}})^2-4\sin^2\mu_{\max}(\sin\alpha+\sin\mu_{\tilde{o}})^2\\ &\quad+(\sin\alpha+\sin\mu_{\tilde{o}})^4+(\cos\alpha-\cos\mu_{\tilde{o}})^4\\ &\quad+4(\cos\alpha-\cos\mu_{\tilde{o}})^2\cos^2\mu_{\max}\\ &\quad+2(\cos\alpha-\cos\mu_{\tilde{o}})^2(\sin\alpha+\sin\mu_{\tilde{o}})^2\\ &\quad+4(\cos\alpha-\cos\mu_{\tilde{o}})(\sin\alpha+\sin\mu_{\tilde{o}})^2\cos\mu_{\max}\\ &\quad+4(\cos\alpha-\cos\mu_{\tilde{o}})^3\cos\mu_{\max}=0. \end{aligned} \tag{48}$$

Or,

$$\begin{aligned} &A^2(\sin\alpha+\sin\mu_{\tilde{o}})^2-4\sin^2\mu_{\max}(\sin\alpha+\sin\mu_{\tilde{o}})^2\\ &\quad+(\sin\alpha+\sin\mu_{\tilde{o}})^4+(\cos\alpha-\cos\mu_{\tilde{o}})^4\\ &\quad+4(\cos\alpha-\cos\mu_{\tilde{o}})^2\cos^2\mu_{\max}\\ &\quad+2(\cos\alpha-\cos\mu_{\tilde{o}})^2(\sin\alpha+\sin\mu_{\tilde{o}})^2\\ &\quad+4(\cos\alpha-\cos\mu_{\tilde{o}})(\sin\alpha+\sin\mu_{\tilde{o}})^2\cos\mu_{\max}\\ &\quad+4(\cos\alpha-\cos\mu_{\tilde{o}})^3\cos\mu_{\max}=0. \end{aligned} \tag{48}$$

This equation can only be solved by numerical methods for $\mu_{\tilde{o}}$. Unfortunately, there usually are two solutions which satisfy this equation. From Table 1, one can see that the spot angular spread is nearly symmetrical around $\mu_{\tilde{o}}=0$.

This research was supported by the Microgravity and Science Applications Division of the National Aeronautics and Space Administration (NASA), Project 963-40-08 (to DCC) and NAS8-39926 (to WMG). EHS is supported by the National Research Council as a research associate. JRR was supported by NASA under contract with Hughes STX. We would like to acknowledge the support of X-ray Optical System, Inc., who provided the prototype convergent optic used in this study. Two of us (SMO and WMG) acknowledge useful discussion with Carolyn MacDonald and other colleagues.

References

Buerger, M. J. (1964). *The Precession Method*. New York: John Wiley.

Colapietro, M., Cappuccio, G., Marciante, C., Pifferi, A., Spagna, R. & Helliwell, J. R. (1992). *J. Appl. Cryst.* **25**, 192–194.

Downing, R. G., Gibson, W. M. & MacDonald, C. A. (1996). *SPIE Proc.* **2859**, 150–161.

Kumakhov, M. A. & Kumarov, F. F. (1990). *Phys. Rep.* **191**(5), 289–350.

Nikonov, S. V. & Chirgadze, Yu. N. (1985). *Acta Cryst.* A**41**, 195–203.

Owens, S. M., Ullrich, J. B., Ponomarev, I. Yu., Carter, D. C., Sisk, R. C., Ho, J. C. & Gibson, W. M. (1996). *SPIE Proc.* **2859**, 200–209.

Snell, E. H., Cassetta, A., Helliwell, J. R., Boggon, T. J., Chayen, N. E., Weckert, E., Hölzer, K., Schroer, K., Gordon, E. J. & Zagalsky, P. F. (1997). *Acta Cryst.* D**53**, 231–239.

Snell, E. H., Weisgerber, S., Helliwell, J. R., Weckert, E., Hölzer, K. & Schroer, K. (1995). *Acta Cryst.* D**51**, 1099–1102.

Ullrich, J. B., Huang, K. G., Owens, S. M., Aloisi, D. C., Hofmann, F. A., Gao, N., Klotzko, I. L. & Gibson, W. M. (1995). *Nucl. Instrum. Methods A*, **364**, 362–367.

Wyckoff, H. W. & Agard, D. (1977). *The Rotation Method in Crystallography*, edited by U. W. Arndt & A. J. Wonacott, pp. 187–206. Amsterdam: North-Holland.

Xiao, Q. F. & Poturaev, S. V. (1994). *Nucl. Instrum. Methods A*, **347**, 376–383.

Xuong, N.-H. & Freer, S. T. (1971). *Acta Cryst.* B**27**, 2380–2387.